Acta Biomaterialia 159 (2023) 338–352

Contents lists available at ScienceDirect

Acta Biomaterialia

journal homepage: www.elsevier.com/locate/actbio

Full length article

Size-optimized nuclear-targeting phototherapy enhances the type I interferon response for “cold” tumor immunotherapy

Xiliu Zhang[a], Chen Yi[a], Lejia Zhang[a], Xinyu Zhu[a], Yi He[a], Huanzi Lu[a], Yiming Li[a], Yuquan Tang[a], Wei Zhao[a], Guosheng Chen[c], Cheng Wang[a,*], Siming Huang[b,*], Gangfeng Ouyang[c], Dongsheng Yu[a,*]

[a] *Hospital of Stomatology, Sun Yat-sen University, Guangdong Provincial Key Laboratory of Stomatology, Guanghua School of Stomatology, Guangzhou, 510055, China*
[b] *Guangzhou Municipal and Guangdong Provincial Key Laboratory of Molecular Target & Clinical Pharmacology, the NMPA and State Key Laboratory of Respiratory Disease, School of Pharmaceutical Sciences and the Fifth Affiliated Hospital, Guangzhou Medical University, Guangzhou 511436, China*
[c] *MOE Key Laboratory of Bioinorganic and Synthetic Chemistry, School of Chemistry, Sun Yat-sen University, Guangzhou 510275, China*

ARTICLE INFO

Article history:
Received 13 September 2022
Revised 5 January 2023
Accepted 9 January 2023
Available online 18 January 2023

Keywords:
Nucleus-targeted
Size-driven
Type I interferon
Photoimmunotherapy
Immune-cold tumor

ABSTRACT

There is growing interest in the effect of innate immune silencing in “cold” tumors, which always fail in the immune checkpoint blockade monotherapy using PD-L1 monoclonal antibodies (aPD-L1). Combination of aPD-L1 with photodynamic therapy, i.e., photoimmunotherapy, is a promising strategy to improve the mono immunotherapy. Nuclear-targeting nanoparticles could elicit a type I interferon (IFN)-mediated innate immune response and reverse the immunosuppressive microenvironment for long-term immunotherapy of “cold” tumors. Photosensitizers such as zinc phthalocyanine (ZnPc) have limited ability to target the nucleus and activate innate sensing pathways to minimize tumor recurrence. Additionally, the relationship between nanoparticle size and nuclear entry capacity remains unclear. Herein, graphene quantum dots (GQDs) were employed as aPD-L1 and ZnPc carriers. Three particle sizes (200 nm, 32 nm and 5 nm) of aPD-L1/ZnPc/GQD-PEG (PZGE) were synthesized and tested. The 5 nm nanoparticles achieved the best nuclear enrichment capacity contributing to their ultrasmall size. Notably, 5 nm PZGE-based photodynamic therapy enabled an amplification of the type I IFN-mediated innate immune response and could convert “immune-cold” tumors into “immune-hot” ones. Utilizing their size advantage to target the nucleus, 5 nm nanoparticles induced DNA damage and activated the type I IFN-mediated innate immune response, subsequently promoting cytotoxic T-lymphocyte infiltration and reversing negative PD-L1 expression. Furthermore, the nanoplatform we designed is promising for the effective suppression of distant oral squamous cell carcinoma. Thus, for the first time, this study presents a size design strategy for nuclear-targeted photo-controlled immune adjuvants and the nuclear-targeted phototherapy-mediated immunomodulatory functions of type I IFN innate immune signalling for “immune-cold” tumors.

Statement of Significance

The potential of commonly used photosensitizers to activate innate sensing pathways for producing type I IFNs is limited due to the lack of nuclear targeting. Facilitating the nuclear-targeting of photosensitizers to enhance innate immune response and execute long-term tumor killing effect would be a promising strategy for “cold” tumor photoimmunotherapy. Herein, we report an optimal size of PZGE nanoparticles that enable the nuclear-targeting of ZnPc, which reinforces the type I IFN-mediated innate immune response, synergistically reversing “cold tumors” to “hot tumors” for effective primary and distant tumor photoimmunotherapy. This work highlights the marked efficacy of ultrasmall nuclear-located nanocarriers and offers new insight into “immune-cold tumors” via prominent innate immune activation mediated by nuclear-targeting photoimmunotherapy.

---

* Correponding authors.
E-mail addresses: wangch75@mail.sysu.edu.cn (C. Wang), huangsm@gzhmu.edu.cn (S. Huang), yudsh@mail.sysu.edu.cn (D. Yu).

https://doi.org/10.1016/j.actbio.2023.01.023
1742-7061/

1. Introduction

Immunotherapy is an active field for the development of antitumor therapies [1,2]. Today, only a small proportion of patients benefit from immunotherapies, mostly those involving immune checkpoint blockades (ICBs), especially programmed death-ligand 1 (PD-L1) [3]. A “cold” tumor microenvironment, which lacks infiltrated cytotoxic T lymphocytes (CTLs) and immune checkpoints expressions, intrinsically limits the efficacy of ICBs therapies [4,5]. Hence, exploring effective approaches to convert “immune cold” tumors into “hot” ones is urgently needed.

Innate immune silencing results in the absence of tumor-infiltrating lymphocytes and negative expression of immune checkpoint [6]. Type I interferons (IFNs) can promote the maturation of dendritic cells (DCs) and cross-presentation of antigens, mediating a wide range of innate immune stimuli [7]. Type I IFNs increase the local concentration of CXCL10, recruiting CD8$^+$ T cells into the tumor bed and enhancing the antitumor T-cell response [8]. Growing evidence indicates that type I IFN-mediated cellular sensor pathway activation can trigger adaptive responses and CTL activity [9,10]. Such innate immune signals play an essential role in recognizing exogenous nucleic acids, especially in the form of cytosolic DNA sensing by the cGAS/STING pathway [11,12].

Among the varieties of remote-control stimuli, photodynamic therapy (PDT) is an archetypical low-toxicity, noninvasive, high-spatiotemporal-controllability method [13–15]. Advancements in nanoplatforms have shown the enhanced permeability and retention effect of photoactivation agents for antitumor phototherapy [16,17]. Nucleus-targeted photosensitizers can exert replication pressure, promote tumor cell apoptosis, and secrete a variety of proinflammatory factors to activate inflammatory cells and induce an antitumor immune response [18,19]. Commonly used photosensitizers are limited in the nuclear targeting and activation of innate sensing pathways for producing type I IFNs [20,21]. Therefore, constructing nuclear-targeting photosensitizers to engage the innate immune response and maximize the long-term tumor killing effect is a potential strategy for “cold” tumor immunotherapy [22,23].

As the regulatory centre of cellular heredity and metabolism, the cell nucleus is a promising subcellular therapeutic location, as an imbalance in metabolism can contribute to the aggressiveness and resistance of cancers [24]. Approaches to target the tumor and cell nucleus could unlock the full potential of tumor phototherapy with limited penetration [25]. Utilizing the quantum dots with small size may be an effective strategy to achieve nuclear targeting. Compared with larger quantum dots, nanoparticles smaller than 10 nm allow more efficient cellular uptake without modifying membrane-penetrating peptides, or other nucleus-targeting molecules [26]. The nanoparticles less than ~5 nm are more inclined to passively diffuse into the nucleus through the nuclear pore complex without special modification [27]. Nevertheless, the nuclear targeting ability of the size effect on tumor cells remains unclear. Hence, we envisage that the rational design of ultrasmall quantum dots, graphene quantum dots (GQDs), may advance the goal of nuclear targeting and photoinduced type I IFN-mediated innate immune response activation, which would be a new approach to priming long-term antitumor immunity. However, such a conceptually new therapeutic strategy has not been explored.

Herein, we loaded zinc phthalocyanine (ZnPc) and PD-L1 molecular antibody (aPD-L1) into GQD-Polyethylene glycol (PEG), which is named as aPD-L1/ZnPc/GQD-PEG (PZGE), to promote the innate immune response and convert an “immune-cold” tumor into an “immune-hot” one. Attributing to the size-driven nuclear-located effect, GQD-PEG facilitated ZnPc penetration and achieved the best intracellular enrichment of tumor nuclei due to its small size (5 nm) compared with the 200 nm and 32 nm nanoparticles. Specifically, photoactivated DNA damage triggered antitumor immunity by activating the STING pathway, followed by immune checkpoint expression upregulation and intertumoral CTL infiltration (Scheme 1). It turned the immune “cold tumor” into a “hot tumor”, showing the benefit of immune checkpoint inhibitor combination therapy. This work provides a precise size-range basis for designing nanomaterials with the ability to target tumor nuclei. Furthermore, it highlights the possibility of nuclear-located nanoparticles for “immune-cold tumor” photoimmunotherapy via a prominent type I IFN-mediated long-term antitumor immune response.

2. Experimental section

2.1. Preparation and characterizations

GQD-PEG nanocarriers with different lateral sizes were synthesized as previously reported [28]. Then, ZnPc (1 mg; TOKYO CHEMICAL INDUSTRY CO., LTD, Tokyo, Japan) was mixed in a purified GQD-PEG (1 mg/mL) aqueous solution, sonicated for 60 min and incubated for 24 h in the dark. Excess ZnPc was removed by filtration through a 7000 Da filter and washed with distilled deionized (DD) water 3 times to obtain the final ZnPc/GQD-PEG products. Specifically, FITC-labelled aPD-L1 was stirred for 6 h and purified by dialysis against DD water for 24 h. Afterwards, the fluorescence-labelled aPD-L1 was added to ZnPc/GQD-PEG under ultrasonic and 24 h gentle stirring. The mixture was centrifuged for 12 h to obtain the final formulation (PZGE). The 200 nm and 32 nm PZGE were synthesized through the similar procedures. The morphology of the nanoparticles was imaged by transmission electron microscopy (TEM; JEM-2010HR, Tokyo, Japan). The zeta potentials were measured with a SZ-100 nanoparticle analyser (Horiba). A fluorescence spectrophotometer (Hitachi, F-2500, Japan) was used to record their fluorescent properties. The protein contents of aPD-L1, ZnPc/GQD-PEG and PZGE were detected using sodium dodecyl sulfate-polyacrylamide gel electrophoresis (SDS-PAGE). Fourier transform infrared (FTIR; ThermoFisher, USA) spectroscopy was used to analyse the elemental composition of the prepared particles. C/N elemental analysis was detected by a Vario EL cube elemental analyser (Elementar, Germany).

2.2. Cell lines and animal model

Human OSCC cell lines SCC9 and SCC25 and human oral keratinocytes (HOKs) were obtained from the American Type Culture Collection (ATCC). The murine SCC cell line SCC-VII was provided by Professor Yixiang Wang (School of Stomatology, Peking University). Cells were cultured in F12/DMEM (SCC9, SCC25, SCCVII) or high glucose/DMEM (HOK) supplemented with 10% FBS, 100 U/ml penicillin–streptomycin and hydrocortisone (400 ng/mL) in an environment of 5% CO_2 at 37°C. Female C3H mice (18~20 g) were obtained from Vital River Laboratory Animal Technology Co., Ltd. (Beijing, China). The OSCC animal model was established by subcutaneous injection of 3.0×10^6 SCCVII cells into the right flank for the primary tumor and 5.0×10^5 SCCVII cells into the left flank for the distant tumor. For the animal experiments, the ethics committee approved the protocol of the Institutional Animal Care and Use Committee (IACUC), Sun Yat-sen University (Approval Number: 2020000640).

2.3. Cellular uptake

The internalization of nanomaterials in different cells was visualized and quantified by confocal laser scanning microscopy (CLSM), a high-content cell imaging system and flow cytometry. To observe the intracellular distribution by CLSM, cells were seeded in the confocal dish and treated with nanoparticles for 12 h before

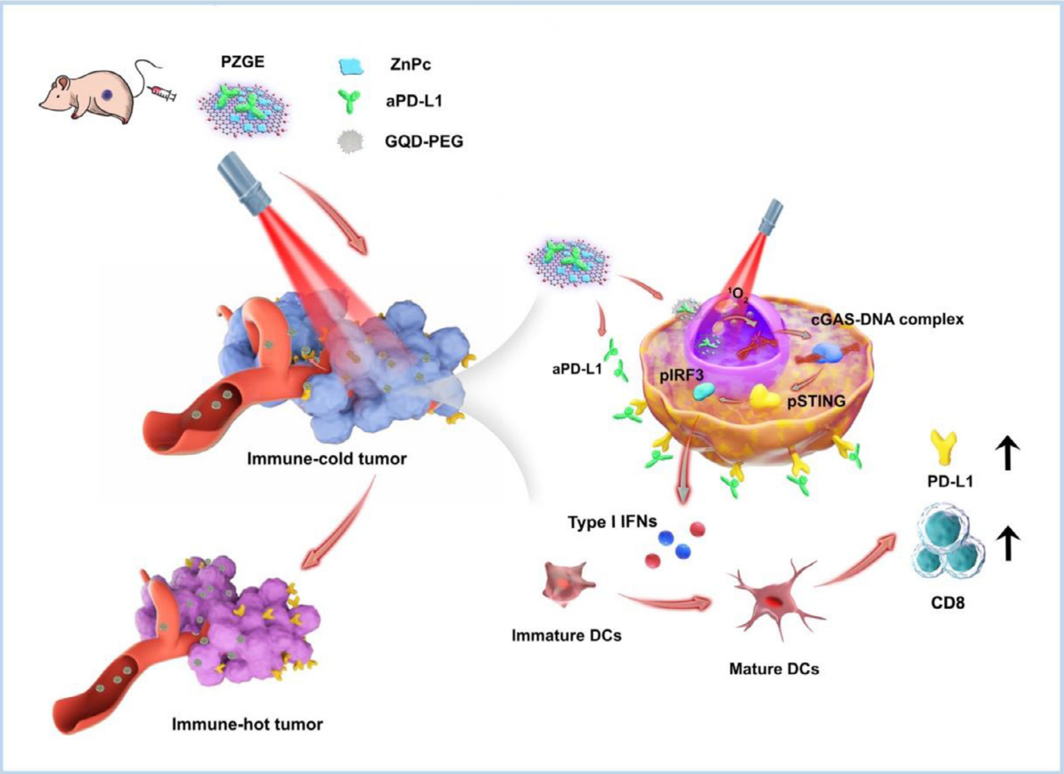

Scheme 1. Schematic illustration of the nuclear-located PZGE nanoparticles for in situ cGAS/STING/IFN I innate immune signalling pathway activation-enhanced "immune-cold tumor" photoimmunotherapy.

being stained with DAPI for nuclei and imaging. Intracellular colocalization was determined with ImageJ. For flow cytometry quantification, cells were seeded into a 6-well plate and incubated with various samples for a certain time. The cells were washed twice with PBS before analysis.

2.4. In vivo imaging and biodistribution

To explore the time-dependent accumulation of PZGE in vivo, real-time fluorescence images of anaesthetized C3H mice were captured by an in vivo imaging system at various time points (12, 24 and 48 h). Finally, their major organs were excised and imaged ex vivo. The average fluorescence intensity results from the images were utilized to analyse the accumulation ability of the nanoparticles in tumors and their biodistribution in major organs.

2.5. In vitro cytotoxicity

To evaluate the biocompatibility of nanomaterials in vitro, a Cell Counting Kit–8 assay (CCK-8; Dojinodo, Tokyo, Japan) was used at various dose concentrations. Tumor cells were seeded into 96-well plates and incubated for 24 h. Then, the cultured medium was replaced with nanoparticles at various concentrations overnight. Before the final detection, cells were cultured with fresh medium for another 24 h. The cell viabilities were determined by the absorbance of 450 nm.

2.6. In vitro phototoxicity

SCC9 and SCC25 cells were seeded in 96-well plates in triplicate (6×10^4 cells/well) and incubated for 24 h. Then the cells were cultured with the prepared materials, followed by laser irradiation (200 mW/cm^2, 8 min). After 24 h of incubation, the cytotoxicity was evaluated by CCK-8 assay and flow cytometry. The Live or Dead^{TM} Cell Viability Assay Kit (AAT Bioquest, American) was used to stain the cells to further visualize the cytotoxicity upon irradiation. Cytosolic DNA damage after irradiation was measured by PicoGreen double-stranded DNA (dsDNA) quantitation reagent staining.

2.7. Singlet oxygen generation

A 670 nm laser (LWRL670-2W-F, Laserware, Beijing, China) was used in the SOSG assay to detect singlet oxygen ($^1O_2$). Cells in 96-well plates were incubated with prepared materials at 25 μg/mL and then irradiated at set time points. The fluorescence signals were detected by fluorometric photometry at the excitation and emission wavelengths of $\lambda_{ex/em}$ = 489 nm/528 nm.

2.8. Immunoblotting

Cells were collected, lysed, separated by SDS-PAGE and transferred to a poly (vinylidene fluoride) membrane. Membranes were incubated in the following primary antibodies (1/1000 dilution) overnight at 4°C: IRF, phospho-IRF, STING, phospho-STING, TBK1, phospho-TBK1, cGAS, PD-L1, γ-H2AX and GAPDH. After incubation with secondary antibodies for 2 h, images were captured using a Li-CorOdyssey-499 Imager.

2.9. Immunofluorescence

Cells or tumor tissues were fixed with 4% paraformaldehyde, permeabilized with 0.1% Triton X-100 and then blocked with BSA. Slices were then incubated with the indicated primary antibodies for 12 h, followed by incubation with Cy3 or FITC-conjugated secondary antibodies. Finally, DAPI was used to stain the nuclei.

The images were visualized using a confocal microscope (Olympus FV3000, Japan).

2.10. Real-time quantitative PCR assay

Total RNA from cells or tumor tissues was extracted with TRIzol (Invitrogen) and then reverse-transcribed with the PrimeScript RT Reagent Kit with gDNA Eraser (Takara). RT-qPCR was performed on a StepOne RT-PCR instrument (ABI Q5) using the SYBR Premix EX Taq Kit (Takara). The $2^{-\Delta\Delta Ct}$ method was used to measure relative expression changes.

2.11. DC maturation in vivo

To detect mature DCs in the lymph nodes, SCC VII-bearing C3H mice were intravenously injected with 200 nm, 32 nm and 5 nm PZGE, respectively. At 24 h postinjection, tumors were exposed to the 200 mW/cm^2 laser. Tumor and tumor-draining lymph nodes were collected on the third day. Single-cell suspension derived from tumor tissues and lymph nodes were stained with anti-CD11c-PC 5.5, anti-MHC II-redFluor 710, anti-CD80-FTIC and CD86-PE antibodies. The antigen presentation-associated cytokines IFN-γ and TNF-α were also examined by the anti-IFN-γ-APC and anti-TNF-α-PE signals.

2.12. PD-L1 expression in vivo

Seven days after laser irradiation, tumors were extracted and digested to single-cell suspensions. To analyse PD-L1 expression in tumor cells and specific lymphocytes, cells were labelled with anti-PD-L1-APC and anti-F4/80-PC 7.

2.13. In vivo therapeutic efficacy

Upon tumor growth to 50 mm^3, mice were randomly divided into five groups ($n = 5$) and administered the indicated samples via tail vein injection every two days for 3 injections. We performed 200 mW/cm^2 670 nm laser irradiation 24 h after sample injection. Tumor volume and body weight were recorded every 2 days until the end of the study. At 14 days postinjection, the tumor and major organs were collected for immunofluorescence and H&E staining. Blood samples were collected and assessed by KingMed Diagnostics Group Co.

2.14. Immune cell infiltration analysis

Tumor and tumor-draining lymph nodes were harvested 14 days after treatment and cut into small pieces. Single-cell suspensions of the tumor were obtained, followed by use of a tumor dissociation kit (Miltenyi Biotec, Germany). After being filtered through a 40 µm cell strainer, the single-cell suspensions were incubated with the following fluorophore-conjugated antibodies: CD45-BV605, CD3-APC/Cy7, CD4-FITC, CD8-PE/Cy7, Foxp3-PE, CD44-PerCP/Cy5.5 and CD62-APC. IFN-γ-APC and TNF-α-PE were also labelled after 6 h of cell activation. The whole-cell suspension was subjected to flow cytometry analysis (BD LSRFortessa).

2.15. Statistical analysis

All the data are presented as mean ± standard error (SE), and comparisons between groups were performed by one-way analysis of variance or Tukey's multiple-comparisons test when appropriate. Statistical significance was defined as $^{*}p < 0.05$, $^{**}\ p < 0.01$, $^{***}\ p < 0.001$ and $^{****}\ p < 0.0001$.

3. Results and discussion

3.1. Synthesis and characterization

Traditional photosensitizers often lack nuclear-targeting ability. Utilizing ultrasmall nanocarriers to enhance the nuclear delivery efficiency of traditional photosensitizers is a potential strategy to overcome this problem. Here, we synthesized ultrasmall PZGE nanoparticles to explore the relationship between the size effect and nuclear internalization (Fig. 1a). Briefly, GQD-PEG was synthesized by taking advantage of the carboxyl groups of GQD, followed by edge PEGylation to enhance its hydrophilicity and biocompatibility as described in our previous report [28,29]. ZnPc, a phthalocyanine derivative, located on the surfaces of GQD-PEG mediated by π-π stacking [30,31]. After ZnPc/GQD-PEG was loaded with aPD-L1, the PZGE nanoparticles exhibited a spherical distribution, as imaged by TEM (Fig. 1b). The average particle size of PZGE was observed to be less than 10 nm (Fig. 1b). We first carried out EDS analysis to demonstrate the formation of PZGE (Fig. 1c). The Zn element originating from ZnPc was presented in the nanostructure. After GQD-PEG was loaded with ZnPc, its zeta potential (Fig. 1d) became less negative (from -21.69 mV to -18.69 mV). The zeta potential of the PZGE nanoparticles was 10.33 mV positive upon successful loading of aPD-L1. These data suggest that aPD-L1 is electrostatically adsorbed on the surface of ZnPc/GQD-PEG. SDS−PAGE showed the successful presence of aPD-L1 on ZnPc/GQD-PEG (Fig. 1e). Under the reducing condition, heavy chain (50 kDa) and light chain (25 kDa) were observed in PZGE group. A non-specific band over 150 kDa in the aPD-L1 lane occurred. This phenomenon might be caused by the partial oxidation or deactivation of the reduction agent during the heating process, leading to the re-association of proteins into the ones larger than the target strip [32]. The IR spectra of PZGE exhibited specific peaks from 1640 cm^{-1} to 1660 cm^{-1}, assigned to the typical amide I band of the polypeptide skeleton (Fig. 1f). The elemental analysis showed that after aPD-L1 loading, the N content increased from 8.55% to 9.42%, accompanied by a decrease in the C/N ratio from 6.71% to 6.02% (Table S1). This N content increase was attributed to aPD-L1 incorporation, giving an ~5.44% wt % aPD-L1 antibody loading. Two distinct absorption peaks of GQD-PEG (at 540 nm) and ZnPc (at 670 nm) were detected in the UV–vis spectrum of PZGE (Fig. 1g). The fluorescence intensity of PZGE was significantly higher than that of free ZnPc, suggesting that the GQD-PEG nanoplatforms reduced the self-quenching effect of ZnPc (Fig. S1). The release profile of aPD-L1 was detected as shown in Fig. S2. Approximately 20% (aPD-L1) release was observed from the PZGE nanoparticles over 24 h, which indicated favourable stability for long-term blood circulation. Additionally, no apparent subsidence phenomenon of PZGE was observed in the different media after seven days, indicating the excellent dispersibility. Together, these results demonstrated that the ultrasmall PZGE nanoparticle was constructed as we expected.

3.2. Particle size optimizes nuclear targeting ability

Currently available photosensitizers in the clinic, such as chlorine e6 [33] and phthalocyanine (PC), have poor cellular-entry capacity, severely limiting their therapeutic efficiency. The particle size of nanomaterials is the key factor in nuclear internalization. However, it is difficult to determine the size range of nanoparticles that will have the best nuclear targeting and tumor enrichment to realize the deep delivery of photoagents [23]. Hence, we synthesized a range of sizes (200 nm, 32 nm and 5 nm) of ZnPc/GQD-PEG and PZGE in the same way to test the size effect on nuclear targeting (Fig. 2a and S3). In the following fluorescence signal analysis, the majority of 5 nm ZnPc/GQD-PEG was distributed

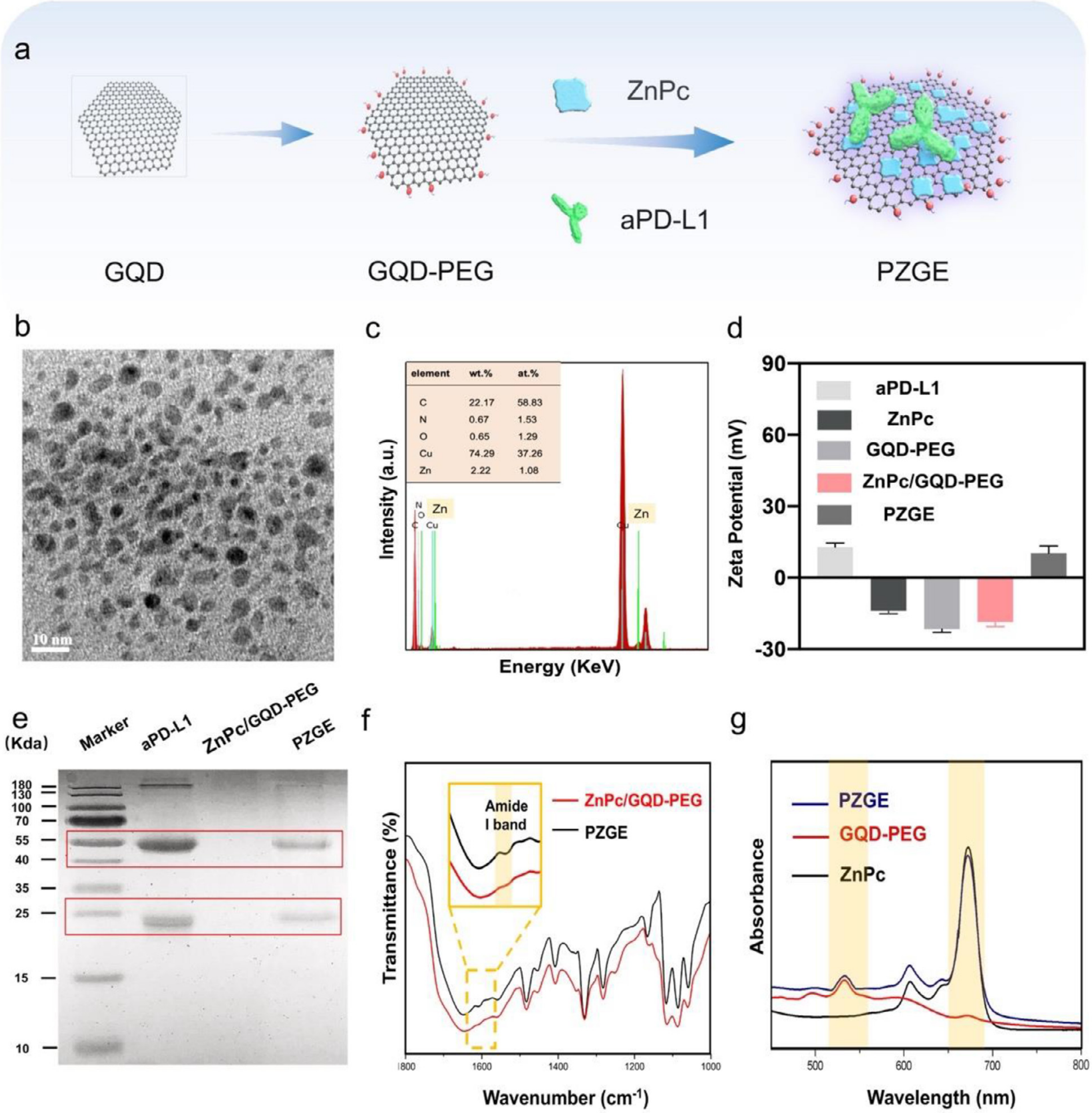

Fig. 1. Characterization of PZGE formulations. (a) Preparation process and (b) TEM image of PZGE. (c) Energy spectrum analysis of ZnPc/GQD-PEG. (d) Zeta potentials of PZGE in water solution. (e) SDS-PAGE quantitative analysis of aPD-L1 antibody modified on ZnPc/GQD-PEG. PZGE includes the typical aPD-L1 protein bands. (f) FT-IR analysis of aPD-L1 antibody loading. FT-IR bands ranging from ~1640 to 1660 cm^{-1} were attributed to the amide I band of the protein. (g) The UV–vis spectra of free ZnPc, GQD-PEG, and PZGE, indicating the successful loading of ZnPc.

inside the nucleus, indicating the superior nucleus-targeting efficiency over that of primary ZnPc (Fig. S4). The nucleocytoplasmic transport of molecular cargoes is mediated by roughly 60-nm-diameter channels in the nuclear envelope, named nuclear pore complexes, which are permeable to molecules with smaller particle sizes [27,34]. ZnPc was codistributed in both the cytoplasm and nucleus in the 32 nm PZGE. In comparison, ZnPc had mostly cytosolic localization in the 200 nm PZGE group (Fig. 2b). Alternatively, the most nuclear-located ZnPc was observed in the 5 nm PZGE group (Fig. S5). With its ultrasmall particle size, 5 nm PZGE could be effectively localized inside the perinuclear region after cellular uptake. This significant nuclear delivery capability mainly relied on passive diffusion mechanism [34]. Compared with free ZnPc localized inside the cytoplasm, the nucleus-targeting property of 5 nm PZGE is most likely related to the ultrasmall particulate dimensions and positively charged amino groups on the surface of these nanoparticles [35]. aPD-L1 (green fluorescence) was mainly located on the cell membrane, and a specific fluorescence signal was observed in the cytoplasm and nucleus, suggesting that when 5 nm PZGE nanoparticles are in the tumor microenvironment, the aPD-L1 loaded on the nanoparticles can bind to the PD-L1 ligand expressed on the tumor cell membrane and thus play a blocking role. At the same time, the binding force between aPD-L1 and PD-L1 on the cell membrane is stronger than the positive and negative charge attraction between aPD-L1 and ZnPc/GQD-PEG, resulting in "self-exudation" in the tumor microenvironment to exert an an-

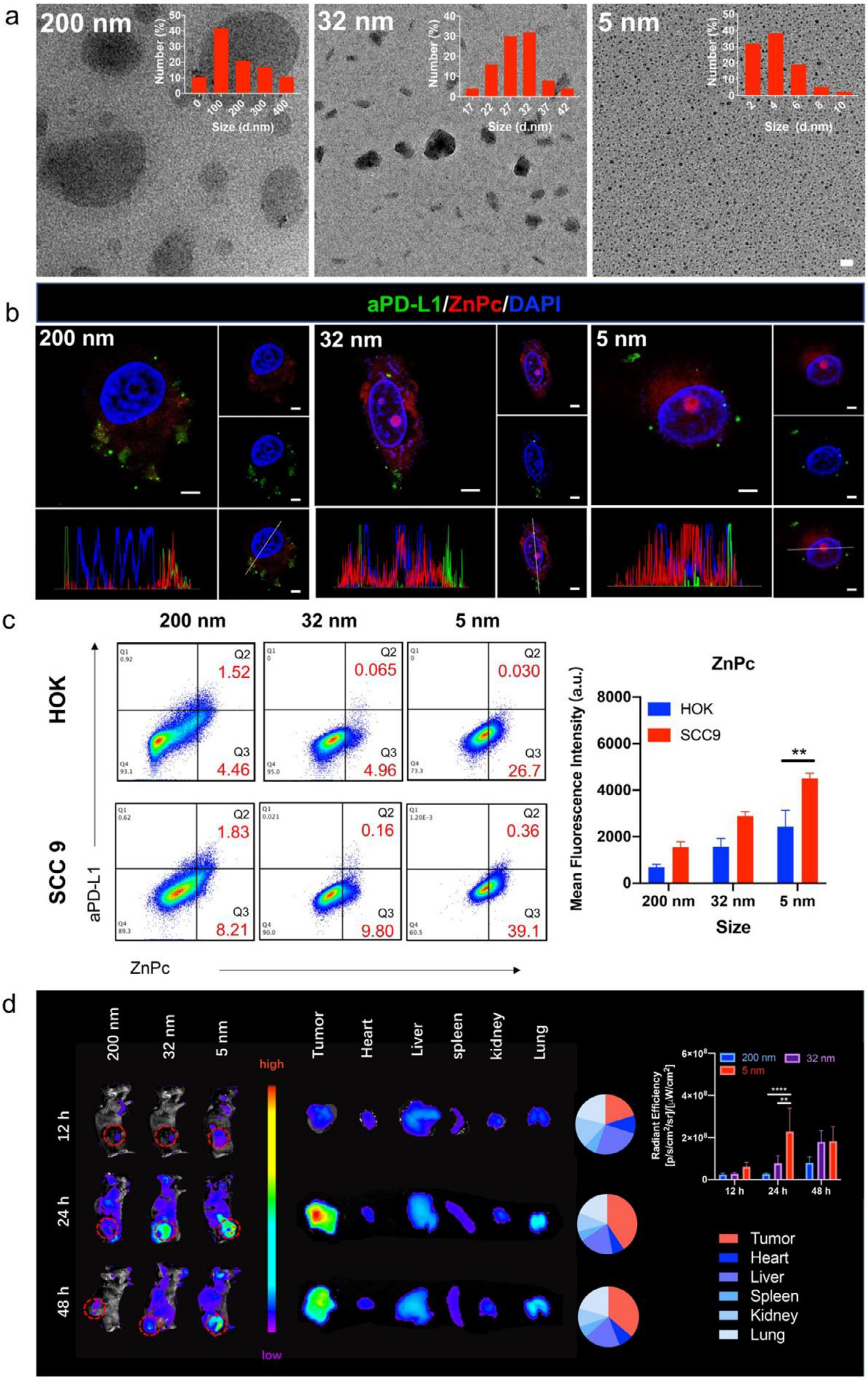

Fig. 2. Size-driven nuclear targeting property of PZGE. (a) TEM images and particle size analysis of 200 nm, 32 nm and 5 nm PZGE. Scare bar = 20 nm. (b) Confocal fluorescence images of SCC9 cells stained with DAPI (nuclear) after incubation with different sized PZGE for 6 h. The corresponding selected linear fluorescence intensity profiles were analysed in the confocal images. Scale bars = 4 μm. (c) Cellular uptake of the different sized nanoparticles by HOK normal cells and SCC 9 tumor cells detected by flow cytometry. (d) In vivo IVIS images of tumor-bearing mice intravenously administered 5 nm PZGE at a series of time points (12, 24, 48 h). Ex vivo IVIS images of excised tumor and organs from corresponding mice and the normalized fluorescence signal of the excised tumor.

tagonistic effect. A certain amount of aPD-L1 was observed in the nucleus, which also indicated that 5 nm ultrasmall nanoparticles may have the potential for nuclear protein transport. Confocal images of the tumor cells were collected for 3D distribution analysis, as displayed in the supplementary movie to investigate the spatiotemporal distribution. The enrichment ability of nanoparticles in normal oral epithelial cells and tumor cells also appeared to have marked differences, especially in the smaller PZGE. As observed in Fig. 2c, the 5 nm PZGE exhibited a higher fluorescence intensity of APC-Cy7 (ZnPc) in tumor cells than in normal cells. This may be due to the overexpressed sialic acid (SA) on the cell membranes of tumor cells. SA is a type of polysaccharide with negative charge composed of a nine-carbon backbone [36], existing at the ends of glycoproteins and glycolipids on the cell membrane surface. Previous reports have discovered that the content of SA on the cell membranes of tumor cells is significantly higher than that of normal cells, leading to higher cellular internalization of nanoparticles with positive charge [37,38]. Thereby, compared to the HOK normal cells, the SCC9 tumor cells were more conducive to the nonselective uptake of positively charged PZGE. The analysis of mean fluorescence intensity further confirmed that 5 nm PZGE significantly enhanced the ZnPc uptake efficiency in tumor cells. The confocal laser also detected the prominent role of the 5 nm size effect on tumor nuclear delivery (Fig. S5). The 5 nm PZGE nanoparticle accomplished the most substantial nuclear penetration, which indicated that the 5 nm ultrasmall size easily broke through the limitation of the nuclear pores, impairing the entry of large, nonspecific entities [34,39]. These results provide a convenient size optimization strategy for the design of nuclear targeted nanoparticles. For these reasons, the solid nuclear-targeted nanocarrier 5 nm ZnPc/GQD-PEG and prepared PZGE were used in the following experiments.

Encouraged by the strong nuclear localization in vitro, the size effect on the tumor targeting efficiency of 5 nm PZGE was investigated in C3H mice by IVIS spectroscopy. Notably, the mice treated with 5 nm PZGE showed stronger fluorescent signals at the tumor lesion than the mice that received PZGE with larger sizes at 12, 24, and 48 hours post intravenous injection (Fig. 2d). Additionally, the highest fluorescent signal in the ex vivo tumor was observed at 24 h, which could last up to 48 h. The natural physical barrier still hinders the effective intertumoral delivery of various compounds [40]. The 5 nm PZGE showed enhanced tumor accumulation, which was greatly attributed to the PEG conjugation and its ultrasmall size, preventing the clearance from reticuloendothelial system (RES). PEGylated interactions could stabilize the nanoparticles and prolong the blood circulation by preventing clearance from the RES [41]. In addition, as shown in Fig. 2d, the liver had a robust fluorescent signal after 5 nm PZGE injection. The reason may be the 1000-fold reduction as the nanomaterials traverse the liver, leading to an essential biological barrier to nanoparticle presentation. Larger nanomaterials are preferentially cleared by the liver, contributing to the macrophage's propensity to phagocytose larger particles. A particle with a lateral size less than 10 nm is less likely to be sequestered in the extrahepatic circulation than in the sinusoid circulation [42]. Meanwhile, the strong fluorescence signals were observed in kidney as well, in accordance with the results that nanoparticles less than 5 nm could be excreted through the urine through glomerular filtration barrier [43]. In addition, studies also indicated that the charge of nanoparticles, water solubility, shape and concentration can also affect the half-life of renal cycle metabolism [44]. In this study, the 5 nm nanoparticle exhibited long-term blood circulation and tumor penetration, which may relate to the size, shape, and concentration of PZGE. Collectively, the cascade tumor-cell targeting and subsequent nucleus traversal by 5 nm PZGE were explored, featuring prominent cell endocytosis and nucleus accumulation.

3.3. Nuclear-targeted PDT enhanced primary and distant OSCC immunotherapy

To explore the effects of nuclear targeting differences on phototoxicity, the high biocompatibility of PZGE with different sizes was first assessed in vitro (Fig. 3a and S6a). Compared with the control group, the cell viability of different sized PZGE groups remained above 80% when their concentration was lower than 100 μg/mL. As displayed in Fig. 3b and S6b, compared with larger sizes, 5 nm PZGE exhibited the strongest phototoxicity upon irradiation, as evaluated by CCK-8 assay. The same results were observed via apoptosis assay (Fig. 3c) and live/dead cell staining (Fig. 3d), which could be attributed to the significantly higher reactive oxygen species (ROS) production efficiency in the tumor cell environment (Fig. S7). Furthermore, the nuclear accumulation of ultrasmall photoagents improved the direct PDT activity by producing the strongly cytotoxic $^1O_2$ around nuclear DNA. This specific characteristic offset the small scope of influence resulting from ROS in phototherapy, which has only a short lifetime (< 0.04 μs) and action radius (< 20 nm) [21].

Given that 5 nm PZGE inhibited OSCC proliferation more effectively in vitro, we hypothesized that nuclear-targeted nanomaterials can induce immunogenetic toxicity in addition to direct antitumor effects and could be more effective in immune combination therapy for distant tumors. The therapeutic efficacy of the formulations was assessed in SCC VII-bearing C3H mice following the therapeutic schedule (Fig. S8a). Size effects on primary tumor phototoxicity were detected first. Of the treatments, 5 nm ZnPc/GQD-PEG with laser had the best antitumor efficiency, indicating that nuclear-targeted phototherapy could maximize the pharmaceutical effect (Fig. 4a-c). Furthermore, as expected, the single PD-L1 antibody or laser treatment showed minimal inhibition, suggesting the importance of photoactivation for effective antitumor immunotherapy (Fig. 4d). Specifically, tumor growth was significantly eliminated in the 5 nm PZGE+L group (Fig. 4e), while the tumor still grew gradually in the 5 nm ZnPc/GQD-PEG treatment group (Fig. 4f). Those nanoparticle treatments led to minimal weight loss as well (Fig. S8b). Long-term recurrence of OSCC is the primary source of treatment failure, so we further tested the therapeutic effect of nanoparticles on distant tumors. After the treatments (Fig. 5a), we observed that the proliferation ability of distant tumors was inhibited by the nuclear-targeted ZnPc/GQD-PEG nanoparticles (Fig. 5b), and the 5 nm PZGE nanoparticles had the best inhibitory effect (Fig. 5c).

The lack of immune cell infiltration in tumor areas was augmented after treatment with 5 nm ZnPc/GQD-PEG. Upon PDT treatment, there was a marked increase in CTL levels (Fig. 5d), showing the successful promotion from "cold tumor" to "hot tumor", a process in which nuclear-targeted nanoparticles played the most vital role [45]. TUNEL staining of the tumor tissue exhibited the strongest cell apoptosis in the ultrasmall photoagents. Further investigation of the immune status in tumor-draining lymph nodes (TDLNs) revealed that many $CD8^+$ cytotoxic T cells were highly infiltrated in the 5 nm nuclear-targeted PZGE group (Fig. 5e). Additionally, a marked decrease was observed in $CD4^+Foxp3^+$T-regulatory (Treg) cells upon treatment with single 5 nm ZnPc/GQD-PEG and 5 nm PZGE with laser (Fig. 5f). Consistent with the antitumor response, treatment with 5 nm PZGE+L significantly upregulated the ratio of $CD8^+$ T cells and Treg cells compared with the control treatment (Fig. 5g). The cytokines TNF-α and IFN-γ increased to 50% and 45% in the 5 nm PZGE group, while almost 10% and 9% in the control group (Fig. 5h and 5i). To better understand the robust antitumor immune response generated after nuclear-located PZGE-mediated PDT treatment, effector memory T cells (Tem) in the spleen were investigated at the end of treatment. The 5 nm PZGE with laser group showed an approximately

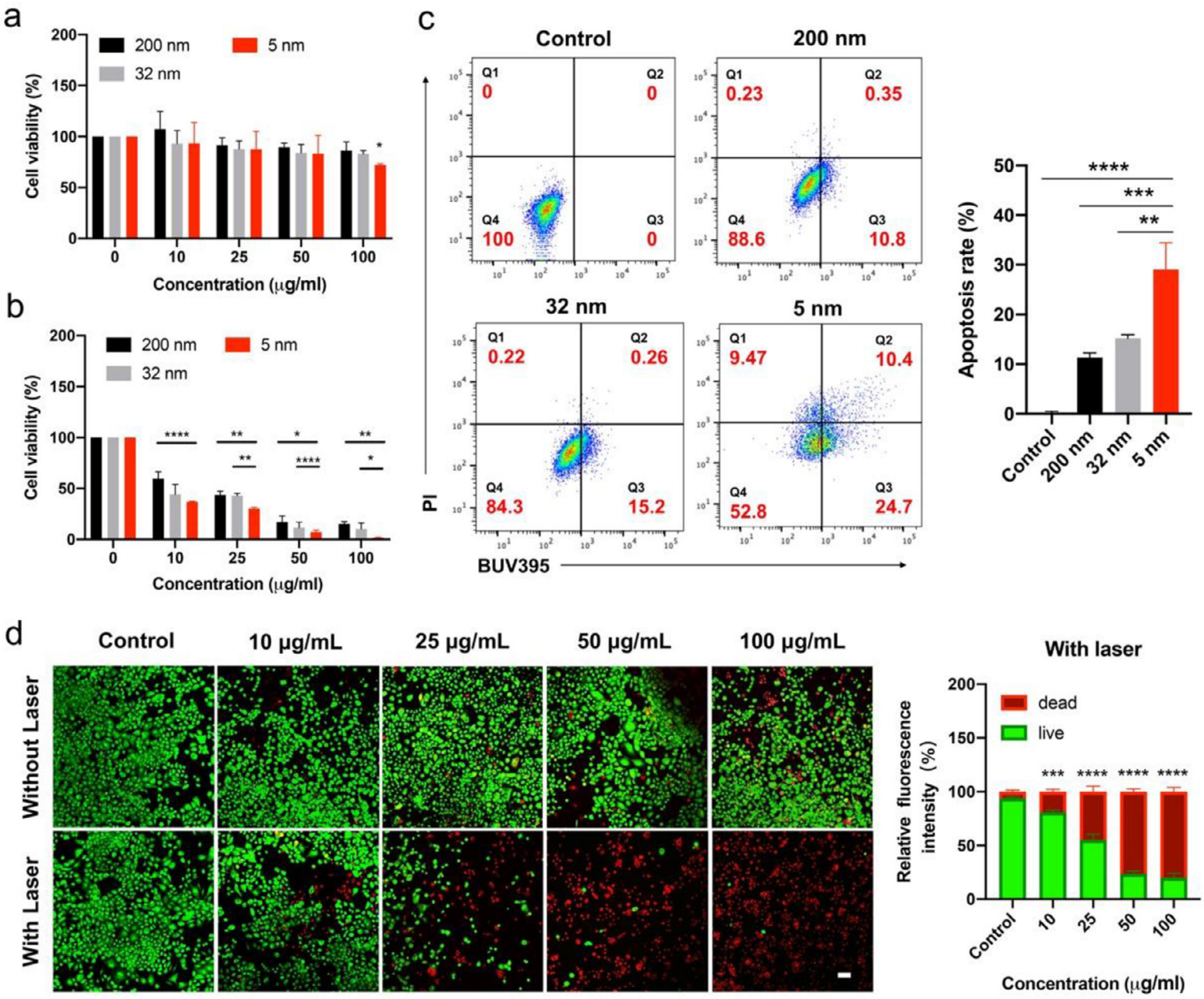

Fig. 3. Nuclear-targeted PZGE enhanced phototoxicity in vitro. (a, b) Cell viability of SCC9 cells incubated with different sized PZGE without laser irradiation (a) or with laser irradiation quantified by CCK-8 assay (b). (c) Apoptosis of SCC25 cells induced by different sized PZGE via flow cytometry. BUV 395 staining was used for early apoptosis and PI staining for late apoptosis. (d) Fluorescence images of SCC25 cells after treatment with PZGE by laser irradiation for 3 min via the live/dead cell staining assays (Calcein-AM/PI). Scale bar = 50 μm.

4-fold increase compared with the control group, which explained its high efficiency in distant antitumor therapy (Fig. 5j).

3.4. Nuclear-targeted PZGE regulates the DNA damage response and activates the cGAS/STING pathway

Innate immune sensors can capture specific molecular patterns derived from tissue damage to alert the adaptive immune system. Normally, the destruction of cellular homeostasis results from DNA damage, dying cells and damaged mitochondria, which induces cytosolic DNA accumulation [46]. dsDNA binds with the major cytosolic nucleic acid sensor cyclic GMP-AMP synthase (cGAS) as well as the downstream stimulator of interferon genes (STING) [47,48]. However, DNA-induced cGAS/STING-mediated type I IFN activation is often suppressed in OSCC [49,50]. Distinct from other larger nanoparticles, 5 nm nanocarriers enhanced the nuclear permeation efficiency of the traditional photosensitizer ZnPc. Thus, nuclear accumulation improved the direct PDT activity by producing primacy cytotoxic $^1O_2$ around nuclear DNA. ROS targeting the nucleus can exert replication pressure, promote tumor cell apoptosis, and secrete a variety of proinflammatory factors to augment the antitumor immune response [21].

In this study, the majority of dsDNA species were seen in the cytosol of 5 nm PZGE-photoactivated cells (Fig. 6a). The 5 nm PZGE significantly promoted the expression of the DNA damage-related marker γ-H2AX compared with the larger size groups, indicating stronger oxidative DNA damage (Fig. 6b) [51,52]. We then examined the expression of the cGAS/STING pathway under photoactivation. As expected, most inflammatory signalling-related proteins, cGAS, p-STING, p-TBK1, and p-IRF3, were dramatically upregulated in tumor cells (Fig. 6b). Recent studies have discovered the underlying mechanism by which DNA damage activates the cGAS/STING pathway and leads to an increase in the inflammatory marker type I IFN. Pathogenic DNA in the nucleus is released into the cytosol during light-associated DNA damage. Numerous cytosolic dsDNA molecules bind to cGAS in the cytosol and activate the adapter protein STING. STING is trafficked from the endoplasmic reticulum to the Golgi apparatus, where it performs activating phosphorylation on TANK-binding kinase 1 (TBK1) and interferon regulatory factor 3 (IRF3), inducing the production of type I IFN and other cytokines [53,54]. The production of two type I IFNs, *IFN-α* and *IFN-β*, was also confirmed by quantitative real-time PCR (RT-qPCR). The 5 nm PZGE induced a 3-fold increase in *IFN-β* and *IFN-α* in tumor cells compared with other groups after laser irradiation, as shown in Fig. 6c. To further validate the type I IFN production mediated

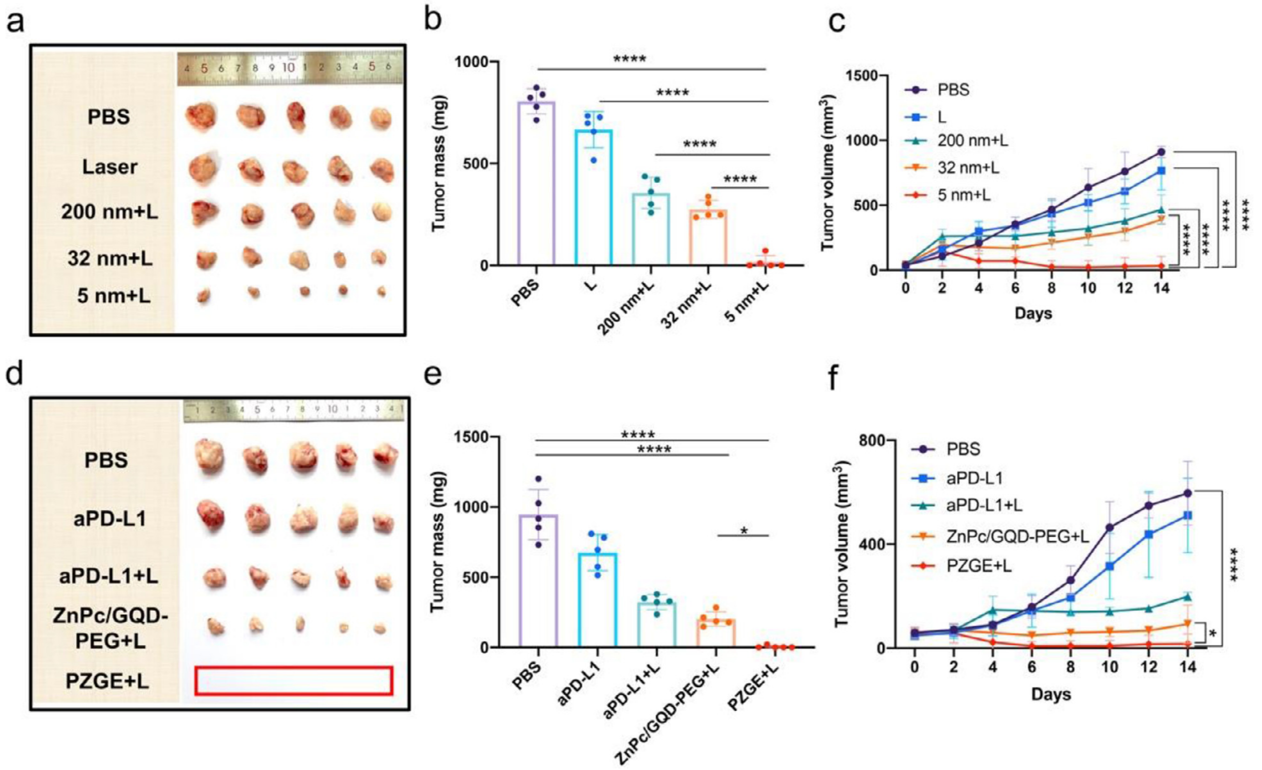

Fig. 4. Nuclear-targeted phototoxicity enhanced primary OSCC immunotherapy. (a, d) Representative images of tumors after different treatments at the end of experiments in the C3H mouse model. (b, e) Tumor weight excised from the C3H mice at the end of the experiment. (c, f) tumor volumes were measured at the indicated time points (n = 5).

by photoinduced cGAS/STING pathway activation, we examined the expression of related proteins in the presence of a cGAS inhibitor (cGASi). Strikingly, PDT-dependent DNA damage and cGAS/STING pathway-related protein expression were significantly suppressed by cGASi (Fig. 6d). In particular, *IFN-α* and *IFN-β* were significantly reduced by 3-fold by the cGAS inhibitor (Fig. 6e). Due to the strongly cytotoxic $^1O_2$ around the nucleus, cGAS/STING pathway-related protein expression and type I IFN production were strikingly upregulated in the 5 nm PZGE group compared with other groups. Together, these data show for the first time that nucleus-targeted nanoparticles can promote ROS production to cause DNA damage, activating the photoinduced dsDNA-cGAS-STING sensing pathway and finally leading to an increase in the production of type I IFN.

3.5. Photoactivated type I interferon-mediated dendritic cell response

Type I IFNs are crucial for antigen presentation by DCs and facilitate the infiltration of tumor-specific CTL and adaptive immunity [55,56]. To explore the underlying mechanism of nuclear-targeted phototoxicity, we next explored whether photoinduced apoptosis could increase type I IFN production in vivo. Three days after irradiation, the expression of γ-H2AX was upregulated, according to the immunofluorescence visualization (Fig. 7a). The 5 nm PZGE group showed enhanced levels of *Ifnb1* and *Ifna* expression, similar to the in vitro results (Fig. 7b and c). Consistent with those findings, both in vitro and in vivo results confirmed the role of tumor-derived dsDNA in phototherapy-induced DNA sensing. The laser induced the accumulation of cytosolic dsDNA in the nuclear-targeted PZGE group, acting on cGAS and leading to downstream STING-mediated type I IFN induction [20]. Then, the production of type I IFNs in an autocrine fashion by tumor cells and host DCs increases the recruitment of tumor-infiltrating DCs and their activation, enhancing antigen cross-presentation and subsequently the antitumor immune response [57]. In addition, host DCs can take up tumor DNA and induce a STING-dependent IFN response, eliciting an antitumor DC response [58].

We then tested the effects of DC activation after phototherapy. Three days after laser irradiation, primary CD11c$^+$MHCII$^+$ DCs were detected in the TDLNs of mice. According to flow cytometry analysis, 5 nm PZGE significantly increased the concentration of mature DCs in the TDLNs. Cell surface expression of costimulatory molecules CD80 and CD86 were slightly increased in TDLNs in the 200 nm group, while the 5 nm PZGE group had significantly higher levels than the 200 nm PZGE group (mean 25% versus 10%, Fig. 7d). The CD80$^+$ DCs and CD86$^+$ DCs were significantly increased under 5 nm PZGE treatment (Fig. 7e and 7f). The secretion of the immune-related cytokines TNF-α and IFN-γ increased by 70% and 60%, respectively, in tumor cells after 5 nm PZGE treatment, to almost twice the levels of the PBS groups (Fig. S9). Increased levels of the proinflammatory cytokines TNF-α and IFN-γ can elicit T-cell activation and host immunity [59]. Myeloid-derived suppressor cells (MDSCs) have been recognized as the major host component in the immunosuppressive tumor microenvironment. Increased MDSC infiltration may promote tumor progression by disrupting host immune surveillance, including direct T-cell inhibition, impairing M1 macrophages and upregulating PD-L1 [60]. Then, as displayed in Fig. 7g, the 5 nm PZGE+L group exhibited an approximately 80% and 30% decrease in MDSCs compared with the 200 nm and 32 nm PZGE groups, respectively. The mechanism of the reduced recruitment of the MDSCs by cGAS/STING/IFN I signal pathway activation has been proved previously [61]. Briefly, independent of IFN-β production, STING overexpression in tumor cells upregulated the suppressor of cytokine signaling 1 (SOCS1), a potent inhibitor of the Janus kinase (JAK)1/2 in the JAK/STAT signaling pathway [62]. It was further established that SOCS1 inter-

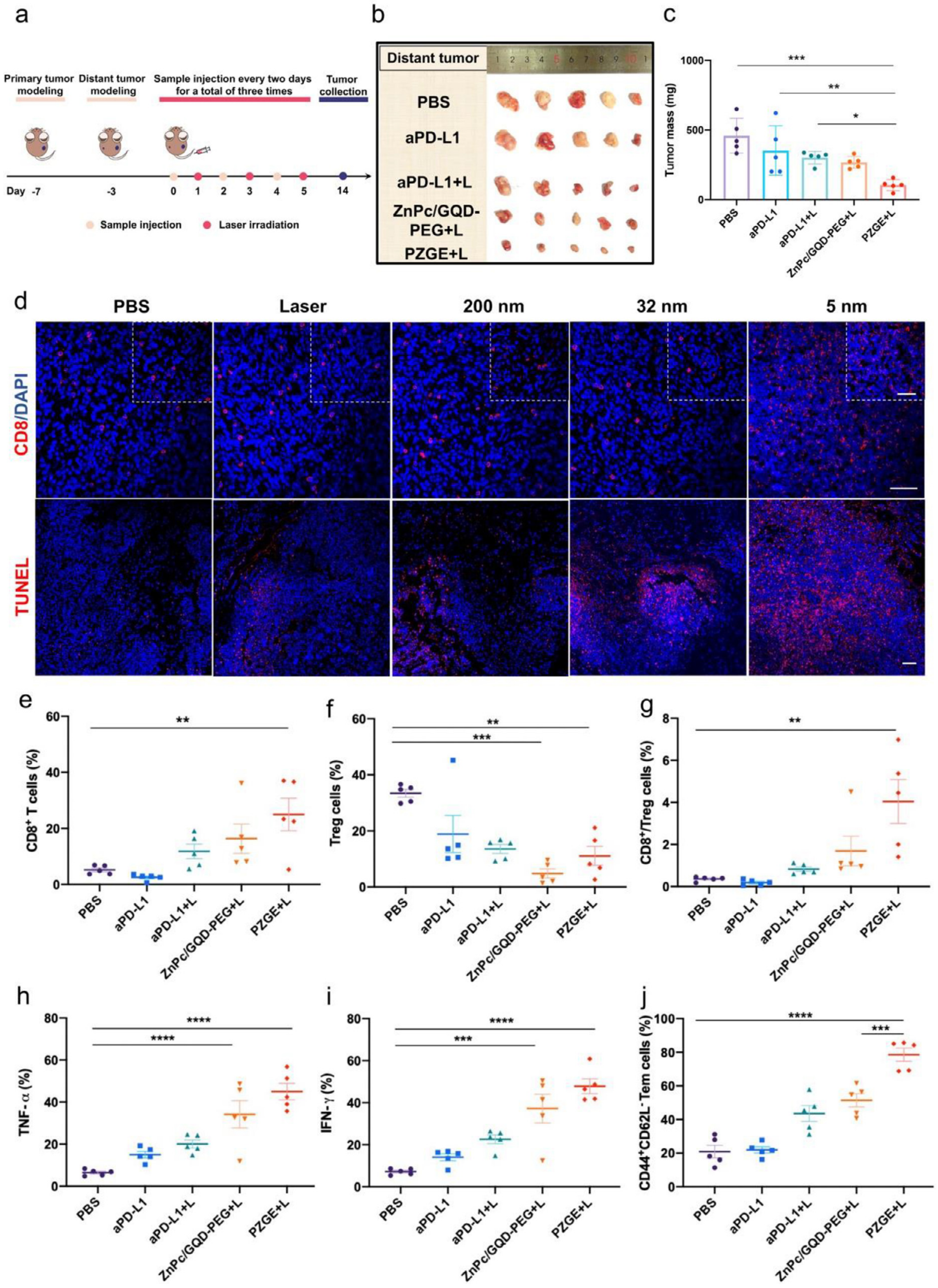

Fig. 5. Nuclear-targeted phototoxicity enhanced distant OSCC immunotherapy. (a) Schematic representation of the experiments. (b) Representative images of tumors after different treatments at the end of experiments in the C3H mouse model. (c) Weight of tumors excised from C3H mice at the end of the experiment. (d) Immunofluorescence signal (red) of $CD8^+$ T cells and TUNEL of representative tumor tissue slices resulting from the different sized ZnPc/GQD-PEG used. Scale bar = 50 μm. (e, f, g) Quantification of $CD8^+$ T cells, $CD4^+Foxp3^+$ Treg cells, and the ratio between $CD8^+$ T cells and Treg cells in each group. (h, i) TNF-α and IFN-γ in $CD8^+$ T cells were detected by flow cytometry. (j) Quantification of the $CD44^+CD62L^-$ Tem cell percentage in the tumor mass. (n = 5).

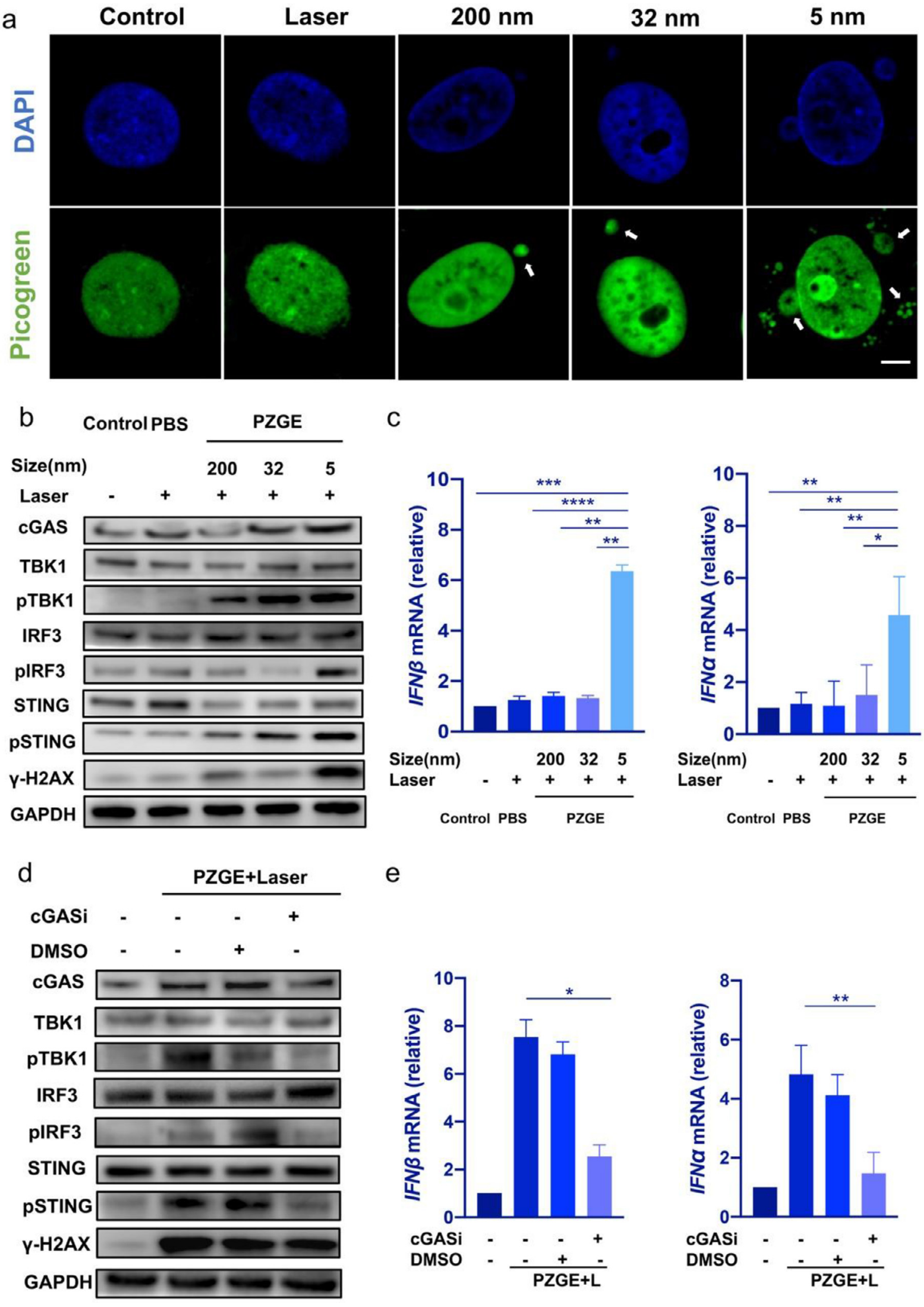

Fig. 6. Nuclear-targeted phototoxicity-induced DNA damage-mediated cGAS/STING/IFN I pathway activation. (a) Representative image of DAPI and PicoGreen staining in SCC25 nuclei after PDT. Scale bar = 5 μm. (b) SCC25 cells were irradiated for 3 min; 24 h later, the cells were collected, and the expression of the indicated proteins was assayed by western blot. (c) SCC9 cells were treated with different formulations for 24 h after irradiation, and cells were collected for *IFNβ* and *IFNα* mRNA detection by RT-qPCR. (d) SCC25 cells were collected from the 5 nm PZGE group, and the indicated proteins were assayed by western blot. (e) SCC9 cells were collected for *IFNβ* and *IFNα* mRNA detection by RT-qPCR. We added 2 μM cGAS inhibitor (cGASi) 2 h prior to PDT induction.

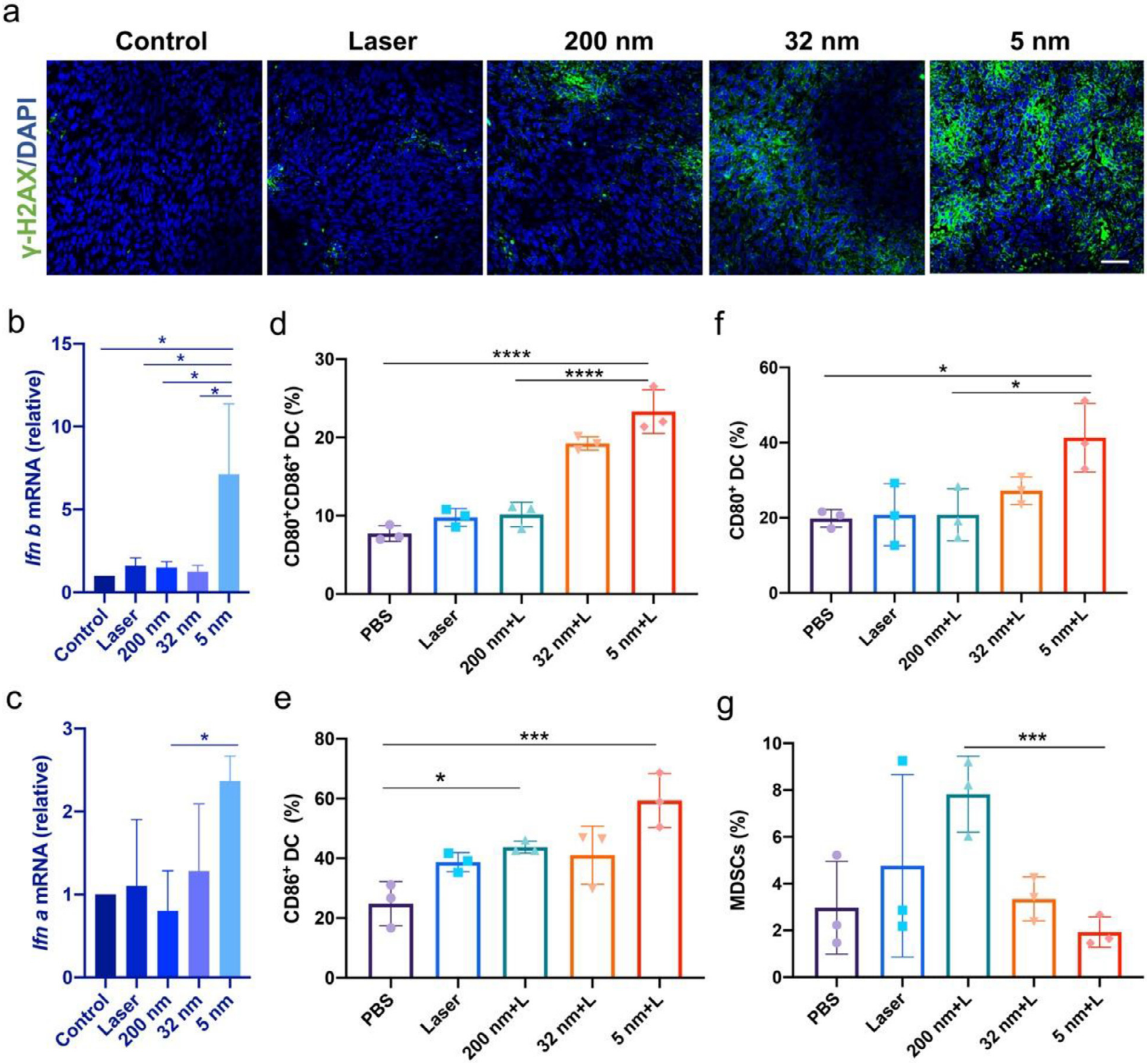

Fig. 7. DC maturation induced by light-mediated interferon pathway activation. (a) Immunohistochemistry (DNA damage marker γ-H2AX) of representative tumor tissue slices from the different treatment groups. Scale bar = 80 μm. (b, c) Seventy-two hours after irradiation, tumors were excised, and RT-qPCR was performed for *Ifnβ* and *Ifnα*. (d, e, f) TDLNs were collected 72 h after irradiation, and the expression of the costimulatory molecules CD80 and CD86 in CD11b$^+$CD11C$^+$MHCII$^+$ DCs was determined by flow cytometry. (g) Flow cytometry analysis of the expression of CD11b$^+$Gr-1$^+$MDSCs in TDLNs extracted from mice 72 h after treatments.

acted directly with STAT3, thereby preventing STAT3 phosphorylation in tumor cells. As a result, the production and release of IL-6 and Granulocyte-macrophage Colony Stimulating Factor (GM-CSF) by tumor cells, two known drivers of MDSC expansion, were inhibited. These results indicate the value of applying nuclear-targeting photoparticles to enhance antigen presentation by promoting DC maturation and MDSC attenuation. Nuclear-targeted PZGE might act as a STING agonist to enhance type I IFN release and DC activation, priming protective antitumor T-cell responses [63].

3.6. Nuclear phototherapy enhances PD-L1 expression for immunotherapy

Despite the great potential for PD-L1 antibody application, lower PD-L1 expression, insufficient T-cell infiltration and reduced antigen presentation have hindered the efficacy of OSCC therapy. It is estimated that over 85% of patients with recurrent or metastatic HNSS have no response to immune checkpoint treatment or have a response that is ultimately followed by disease progression and death from the disease [1]. Here, we found that nuclear-targeted nanoparticles could regulate PD-L1 expression to reverse the immunosuppressive microenvironment.

To evaluate whether PD-L1 is involved in immune surveillance in nucleus-targeted phototherapy, we detected the expression of PD-L1 in vitro and in vivo. In the in vitro experiments, the most significant degree of PD-L1 upregulation was seen in the 5 nm ZnPc/GQD-PEG groups according to the western blot results (Fig. 8a and b). Seven days after phototherapy in vivo, the 5 nm ZnPc/GQD-PEG groups exhibited the most marked PD-L1 change (up to 2-fold) in tumor cells compared with the control group (Fig. 8c). Furthermore, PD-L1 increased in DCs (up to 3-fold) and macrophages (up to 3-fold) compared with its levels the control group (Fig. 8d). Though the higher expression of PD-L1 on tumor cells is positively correlated with a better immune response, some PD-L1-negative patients still respond to antibody blockade [64]. Recent findings suggested that PD-L1 expressed in host myeloid cells is essential for the response to checkpoint blockade, especially in antigen presenting cells (APCs) [65]. The expression of PD-L1 in DCs in the tu-

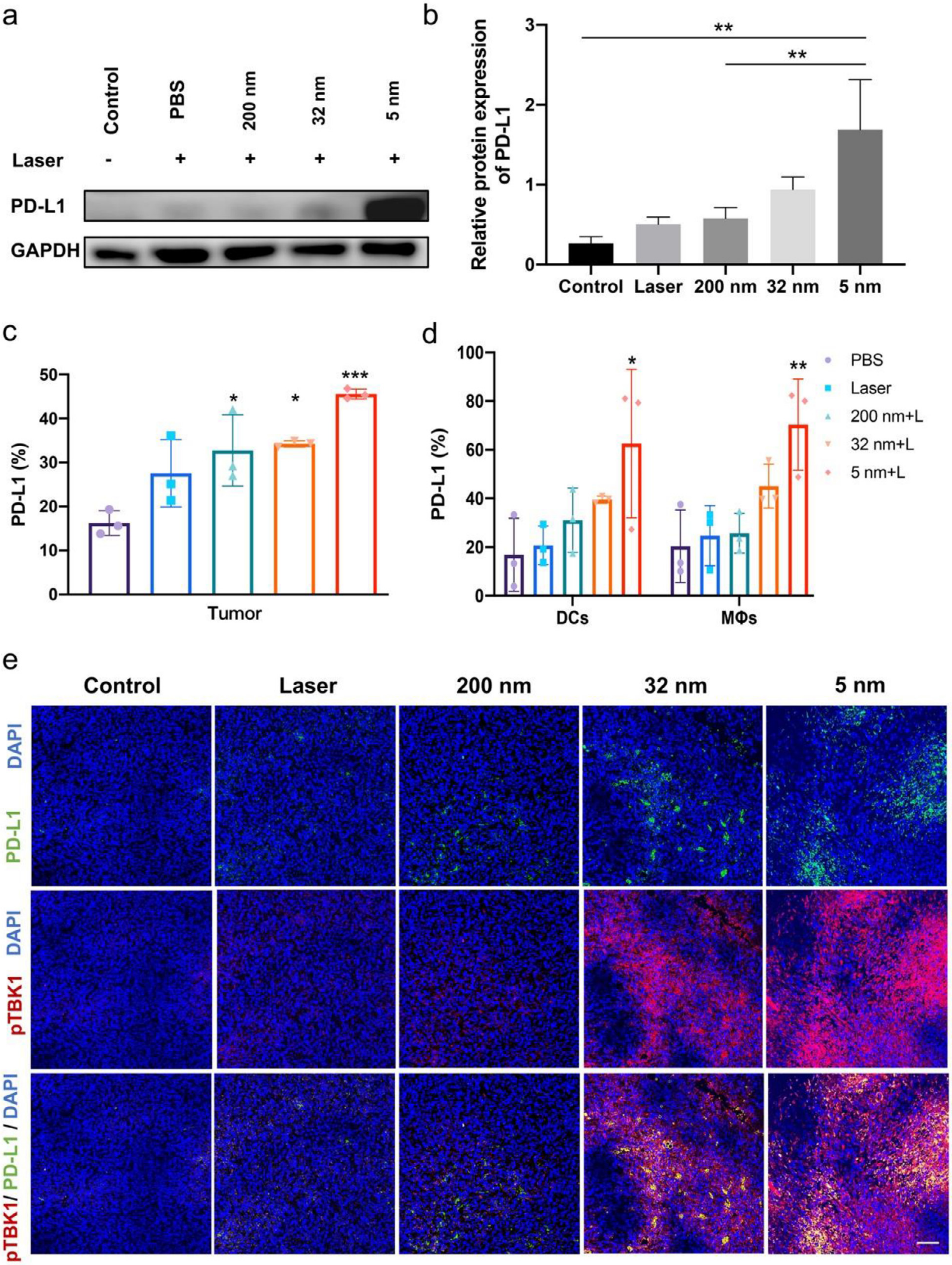

Fig. 8. Nuclear targeted photodynamic therapy upregulates PD-L1 expression. (a, b) In vitro PD-L1 expression in SCC9 cells was examined 24 h after different treatments and analysed by ImageJ. PD-L1 expression was measured by flow cytometry in (c) tumor cells and (d) immune cell subsets in tumor tissues after 7 days of irradiation in vivo. (e) Immunohistochemistry (PD-L1 and pTBK1) of representative tumor tissue slices from the different treatment groups. Scale bar = 80 μm.

mor microenvironment was much higher than that of tumor cells, and when the PD-L1 in DC was knocked out, the effect of PD-L1 blocking therapy completely disappeared [66]. Meanwhile, studies have confirmed that PD-L1$^+$ macrophages infiltrated in tumors are also related to the efficacy of aPD-L1. Studies have found in nearly 500 cancer cases that 80% of CD68$^+$ macrophages express PD-L1, and these patients have longer overall survival during aPD-L1 treatment [67]. Immunofluorescence showed the most significant PD-L1 expression in the 5 nm ZnPc/GQD-PEG groups, according to p-TBK1 and γ-H2AX expression (Fig. 8e). Lower PD-L1 expression, insufficient T-cell infiltration, and reduced antigen presentation hinder PD-L1 antibody efficacy in OSCC therapy. Recent discoveries have shown that PD-L1 expression in cancer cells is upregulated by DNA damage signalling. Oxidative stress-mediated DNA double-strand breaks (DSBs) enhance PD-L1 expression [9]. Positive tumor-presenting neoantigens can promote the release of IFN-γ to enhance PD-L1 expression under oxidative stress [68]. Sen *et al.* injected cGAS- or STING-depleted tumor cells into immune-competent mice to detect the role of cGAS-mediated STING activation in the DNA damage repair-PD-L1 blockade combination effect [69]. They found that both cGAS-knockdown and STING-knockdown tumors progressed even with PD-L1 and DNA damage repair protein (CHK1/PARP) inhibitors. Positive tumor-presenting neoantigens promote the release of IFN-γ to enhance PD-L1 expression under oxidative stress [68]. The results above show that these ultrasmall photoagents had a better antitumor effect than larger photoagents. Importantly, this nuclear-targeted phototherapy can convert an “immune-cold” tumor into a “hot” one, suggesting a strategy for vaccine design involving photoimmunotherapy that would be maximally efficient.

The bioadaptability of different sized PZEG was systematically detected by haematology and blood biochemistry after intravenous injection. As observed in H&E staining images (Fig. S10), the major organ sections excised from various formulation treatments exhibited no obvious histopathological abnormalities. Moreover, all the measured blood biochemistry parameters and complete panel data for different materials exhibited negligible changes, indicating the potential long-term biocompatibility of PZGE nanoparticles (Fig. S11).

4. Conclusion

We report an optimal size of nuclear-targeting PZGE nanoparticles to reinforce the type I IFN-mediated innate immune response, synergistically contributing to reversing “cold tumors” for effective primary and distant tumor photoimmunotherapy. In particular, this ultrasmall 5 nm nanoparticle reverses low PD-L1 expression via nuclear-located PDT-mediated DNA damage. Then, photoinduced cGAS/STING/IFN I pathway activation upregulates DC maturation and CTL infiltration, significantly increasing the long-term immunotherapeutic efficiency of “immune-cold” tumors. This work highlights the marked efficacy of smaller nuclear-located nanocarriers and offers new insight into “immune-cold tumors” via prominent innate immune activation mediated by nuclear-targeting photoimmunotherapy.

Declaration of Competing Interest

The authors declare that they have no known competing financial interests that could have appeared to influence this work.

Acknowledgements

This work was supported by the National Natural Science Foundation of China (Nos. 82073378, 81873711, 81974146) and the Natural Science Foundation of Guangdong Province (2021A1515012399).

Supplementary materials

Supplementary material associated with this article can be found, in the online version, at doi:10.1016/j.actbio.2023.01.023.

References

[1] L.Q.M. Chow, Head and neck cancer, New Engl. J. Med. 382 (1) (2020) 60–72.
[2] N. Gavrielatou, S. Doumas, P. Economopoulou, P.G. Foukas, A. Psyrri, Biomarkers for immunotherapy response in head and neck cancer, Cancer Treat. Rev. 84 (2020) 101977.
[3] J.R. Brahmer, S.S. Tykodi, L.Q. Chow, W.J. Hwu, S.L. Topalian, P. Hwu, C.G. Drake, L.H. Camacho, J. Kauh, K. Odunsi, H.C. Pitot, O. Hamid, S. Bhatia, R. Martins, K. Eaton, S. Chen, T.M. Salay, S. Alaparthy, J.F. Grosso, A.J. Korman, S.M. Parker, S. Agrawal, S.M. Goldberg, D.M. Pardoll, A. Gupta, J.M. Wigginton, Safety and activity of anti-PD-L1 antibody in patients with advanced cancer, New Engl. J. Med 366 (26) (2012) 2455–2465.
[4] J.W. Carlisle, C.E. Steuer, T.K. Owonikoko, N.F. Saba, An update on the immune landscape in lung and head and neck cancers, CA. Cancer J. Clin. 70 (6) (2020) 505–517.
[5] E.E.W. Cohen, R.B. Bell, C.B. Bifulco, B. Burtness, M.L. Gillison, K.J. Harrington, Q.T. Le, N.Y. Lee, R. Leidner, R.L. Lewis, L. Licitra, H. Mehanna, L.K. Mell, A. Raben, A.G. Sikora, R. Uppaluri, F. Whitworth, D.P. Zandberg, R.L. Ferris, The Society for Immunotherapy of Cancer consensus statement on immunotherapy for the treatment of squamous cell carcinoma of the head and neck (HNSCC), J. Immunother. Cancer 7 (1) (2019) 184.
[6] G.M. Boukhaled, R. Gadalla, H.J. Elsaesser, D. Abd-Rabbo, R. Quevedo, S.Y.C. Yang, M. Guo, B.X. Wang, B. Noamani, D. Gray, S.C.M. Lau, K. Taylor, K. Aung, A. Spreafico, A.R. Hansen, S.D. Saibil, N. Hirano, C. Guidos, T.J. Pugh, T.L. McGaha, P.S. Ohashi, A.G. Sacher, M.O. Butler, D.G. Brooks, Pre-encoded responsiveness to type I interferon in the peripheral immune system defines outcome of PD1 blockade therapy, Nat. Immunol. 23 (8) (2022) 1273–1283.
[7] R. Yu, B. Zhu, D. Chen, Type I interferon-mediated tumor immunity and its role in immunotherapy, Cell. Mol. Life Sci. 79 (3) (2022) 191.
[8] M. Liu, M.S. Etherington, A. Hanna, B.D. Medina, G.A. Vitiello, T.G. Bowler, N.J. Param, L. Levin, F. Rossi, R.P. DeMatteo, Oncogenic KIT Modulates Type I IFN-Mediated Antitumor Immunity in GIST, Cancer Immunol. Res. 9 (5) (2021) 542–553.
[9] H. Sato, A. Niimi, T. Yasuhara, T.B.M. Permata, Y. Hagiwara, M. Isono, E. Nuryadi, R. Sekine, T. Oike, S. Kakoti, Y. Yoshimoto, K.D. Held, Y. Suzuki, K. Kono, K. Miyagawa, T. Nakano, A. Shibata, DNA double-strand break repair pathway regulates PD-L1 expression in cancer cells, Nat. Commun. 8 (1) (2017) 1751.
[10] S. Yum, M. Li, Z.J. Chen, Old dogs, new trick: classic cancer therapies activate cGAS, Cell. Res. 30 (8) (2020) 639–648.
[11] Y. Wang, J. Luo, A. Alu, X. Han, Y. Wei, X. Wei, cGAS-STING pathway in cancer biotherapy, Mol. Cancer 19 (1) (2020) 136.
[12] M.Z. Zou, Z.H. Li, X.F. Bai, C.J. Liu, X.Z. Zhang, Hybrid vesicles based on autologous tumor cell membrane and bacterial outer membrane to enhance innate immune response and personalized tumor immunotherapy, Nano. Lett. 21 (20) (2021) 8609–8618.
[13] Z. Zeng, C. Zhang, J. Li, D. Cui, Y. Jiang, K. Pu, Activatable polymer nanoenzymes for photodynamic immunometabolic cancer therapy, Adv. Mater. (2020) e2007247.
[14] Y. Liu, W. Zhen, Y. Wang, S. Song, H. Zhang, Na2S2O8 nanoparticles trigger antitumor immunotherapy through reactive oxygen species storm and surge of tumor osmolarity, J. Am. Chem. Soc. 142 (52) (2020) 21751–21757.
[15] X. Zhang, J. Tang, C. Li, Y. Lu, L. Cheng, J. Liu, A targeting black phosphorus nanoparticle based immune cells nano-regulator for photodynamic/photothermal and photo-immunotherapy, Bioact. Mater. 6 (2) (2021) 472–489.
[16] Z. Guo, Y. Hu, M. Zhao, K. Hao, P. He, H. Tian, X. Chen, M. Chen, Prodrug-based versatile nanomedicine with simultaneous physical and physiological tumor penetration for enhanced cancer chemo-immunotherapy, Nano Lett. 21 (9) (2021) 3721–3730.
[17] M. Tavakkoli Yaraki, M. Wu, E. Middha, W. Wu, S. Daqiqeh Rezaei, B. Liu, Y.N. Tan, Gold nanostars-AIE theranostic nanodots with enhanced fluorescence and photosensitization towards effective image-guided photodynamic therapy, Nano-Micro Lett. 13 (1) (2021) 58.
[18] Y. Wang, S. Luo, Y. Wu, P. Tang, J. Liu, Z. Liu, S. Shen, H. Ren, D. Wu, Highly penetrable and on-demand oxygen release with tumor activity composite nanosystem for photothermal/photodynamic synergetic therapy, ACS Nano 14 (2020) 17046–17062.
[19] M. Chen, S. Hu, Y. Li, T.T. Jiang, H. Jin, L. Feng, Targeting nuclear acid-mediated immunity in cancer immune checkpoint inhibitor therapies, Signal Transduct. Target. Ther. 5 (1) (2020) 270.
[20] J. Chen, S.M. Harding, R. Natesan, L. Tian, J.L. Benci, W. Li, A.J. Minn, I.A. Asangani, R.A. Greenberg, Cell cycle checkpoints cooperate to suppress DNA- and RNA-associated molecular pattern recognition and anti-tumor immune responses, Cell Rep. 32 (9) (2020) 108080.
[21] Q. Zhan, X. Shi, D. Fan, L. Zhou, S. Wei, Solvent mixing generating air bubbles as a template for polydopamine nanobowl fabrication: Underlying mechanism, nanomotor assembly and application in cancer treatment, Chem. Eng. J. 404 (2021) 126443.
[22] S. Gou, W. Liu, S. Wang, G. Chen, Z. Chen, L. Qiu, X. Zhou, Y. Wu, Y. Qi, Y. Gao, Engineered nanovaccine targeting Clec9a(+) dendritic cells remarkably

enhances the cancer immunotherapy effects of STING agonist, Nano Lett. 21 (23) (2021) 9939–9950.

[23] Y. Wang, Y. Tang, Y. Du, L. Lin, Z. Zhang, X. Ou, S. Chen, Q. Wang, J. Zou, Genetically engineered bacteria-mediated multi-functional nanoparticles for synergistic tumor-targeting therapy, Acta Biomater. 150 (2022) 337–352.

[24] Z.E. Stine, Z.T. Schug, J.M. Salvino, C.V. Dang, Targeting cancer metabolism in the era of precision oncology, Nat. Rev. Drug. Discov 21 (2) (2022) 141–162.

[25] R. Jing, Q. Wang, L. Chen, G. Li, R. Li, L. Zhang, H. Zhang, B. Zuo, Y. Seow, X. Qiao, B. Wang, J. Xu, J. Chen, T. Song, H. Yin, Functional imaging and targeted drug delivery in mice and patient tumors with a cell nucleolus-localizing and tumor-targeting peptide, Biomaterials 289 (2022) 121758.

[26] X. Li, M. Zha, Y. Li, J.S. Ni, T. Min, T. Kang, G. Yang, H. Tang, K. Li, X. Jiang, Sub-10 nm aggregation-induced emission quantum dots assembled by microfluidics for enhanced tumor targeting and reduced retention in the liver, Angew Chem. Int. Ed. 59 (49) (2020) 21899–21903.

[27] C. Zelmer, L.P. Zweifel, L.E. Kapinos, I. Craciun, Z.P. Guven, C.G. Palivan, R.Y.H. Lim, Organelle-specific targeting of polymersomes into the cell nucleus, Proc. Natl. Acad. Sci. USA 117 (6) (2020) 2770–2778.

[28] X. Zhang, H. Li, C. Yi, G. Chen, Y. Li, Y. Zhou, G. Chen, Y. Li, Y. He, D. Yu, Host immune response triggered by graphene quantum-dot-mediated photodynamic therapy for oral squamous cell carcinoma, Int. J. Nanomed. 15 (2020) 9627–9638.

[29] X. Zhang, C. Wei, Y. Li, D. Yu, Shining luminescent graphene quantum dots: synthesis, physicochemical properties, and biomedical applications, TrAC-Trend. Anal. Chem. 116 (2019) 109–121.

[30] D. Du, K. Wang, Y. Wen, Y. Li, Y.Y. Li, Photodynamic graphene quantum dot: reduction condition regulated photoactivity and size dependent efficacy, ACS Appl. Mater. Interfaces 8 (5) (2016) 3287–3294.

[31] S. Li, S. Zhou, Y. Li, X. Li, J. Zhu, L. Fan, S. Yang, Exceptionally high payload of the IR780 iodide on folic acid-functionalized graphene quantum dots for targeted photothermal therapy, ACS Appl. Mater. Interfaces 9 (27) (2017) 22332–22341.

[32] M. Kalim, J. Chen, S. Wang, C. Lin, S. Ullah, K. Liang, Q. Ding, S. Chen, J. Zhan, Construction of high level prokaryotic expression and purification system of PD-L1 extracellular domain by using Escherichia coli host cell machinery, Immunol. Lett. 190 (2017) 34–41.

[33] L.P. Zhao, R.R. Zheng, J.Q. Huang, X.Y. Chen, F.A. Deng, Y.B. Liu, C.Y. Huang, X.Y. Yu, H. Cheng, S.Y. Li, Self-delivery photo-immune stimulators for photodynamic sensitized tumor immunotherapy, ACS Nano 14 (12) (2020) 17100–17113.

[34] B.L. Timney, B. Raveh, R. Mironska, J.M. Trivedi, S.J. Kim, D. Russel, S.R. Wente, A. Sali, M.P. Rout, Simple rules for passive diffusion through the nuclear pore complex, J. Cell Biol. 215 (1) (2016) 57–76.

[35] L. Wang, T. Zhang, M. Huo, J. Guo, Y. Chen, H. Xu, Construction of nucleus-targeting iridium nanocrystals for photonic hyperthermia-synergized cancer radiotherapy, Small 15 (47) (2019) e1903254.

[36] X.J. Shi, S.H.P. Sung, J.H.C. Chau, Y. Li, Z.Y. Liu, R.T.K. Kwok, J.K. Liu, P.H. Xiao, J.J. Zhang, B. Liu, J.W.Y. Lam, B.Z. Tang, Killing G(+) or G(-) bacteria? The important role of molecular charge in AIE-active photosensitizers, Small Methods 4 (7) (2020).

[37] M.R. Hamblin, J.L. Miller, I. Rizvi, H.G. Loew, T. Hasan, Pegylation of charged polymer-photosensitiser conjugates: effects on photodynamic efficacy, Br. J. Cancer 89 (5) (2003) 937–943.

[38] K. Li, C.J. Liu, X.Z. Zhang, Multifunctional peptides for tumor therapy, Adv. Drug Deliv. Rev. 160 (2020) 36–51.

[39] Y.X. Zhu, H.R. Jia, G.Y. Pan, N.W. Ulrich, Z. Chen, F.G. Wu, Development of a light-controlled nanoplatform for direct nuclear delivery of molecular and nanoscale materials, J. Am. Chem. Soc. 140 (11) (2018) 4062–4070.

[40] S. Sindhwani, A.M. Syed, J. Ngai, B.R. Kingston, L. Maiorino, J. Rothschild, P. MacMillan, Y. Zhang, N.U. Rajesh, T. Hoang, J.L.Y. Wu, S. Wilhelm, A. Zilman, S. Gadde, A. Sulaiman, B. Ouyang, Z. Lin, L. Wang, M. Egeblad, W.C.W. Chan, The entry of nanoparticles into solid tumours, Nat. Mater. 19 (5) (2020) 566–575.

[41] B. Feng, B. Hou, Z. Xu, M. Saeed, H. Yu, Y. Li, Self-amplified drug delivery with light-inducible nanocargoes to enhance cancer immunotherapy, Adv. Mater. 31 (40) (2019) e1902960.

[42] K.M. Tsoi, S.A. MacParland, X.Z. Ma, V.N. Spetzler, J. Echeverri, B. Ouyang, S.M. Fadel, E.A. Sykes, N. Goldaracena, J.M. Kaths, J.B. Conneely, B.A. Alman, M. Selzner, M.A. Ostrowski, O.A. Adeyi, A. Zilman, I.D. McGilvray, W.C. Chan, Mechanism of hard-nanomaterial clearance by the liver, Nat. Mater. 15 (11) (2016) 1212–1221.

[43] I.S. Daehn, J.S. Duffield, The glomerular filtration barrier: a structural target for novel kidney therapies, Nat. Rev. Drug Discov. 20 (10) (2021) 770–788.

[44] J. Xu, M.X. Yu, C.Q. Peng, J. Zheng, Dose dependencies and biocompatibility of renal clearable gold nanoparticles: from mice to non-human primates, Abstr. Pap. Amer. Chem. Soc. 256 (2018).

[45] J. Galon, D. Bruni, Approaches to treat immune hot, altered and cold tumours with combination immunotherapies, Nat. Rev. Drug Discov. 18 (3) (2019) 197–218.

[46] A. Takahashi, T.M. Loo, R. Okada, F. Kamachi, Y. Watanabe, M. Wakita, S. Watanabe, S. Kawamoto, K. Miyata, G.N. Barber, N. Ohtani, E. Hara, Downregulation of cytoplasmic DNases is implicated in cytoplasmic DNA accumulation and SASP in senescent cells, Nat. Commun. 9 (1) (2018) 1249.

[47] K.J. Mackenzie, P. Carroll, C.A. Martin, O. Murina, A. Fluteau, D.J. Simpson, N. Olova, H. Sutcliffe, J.K. Rainger, A. Leitch, R.T. Osborn, A.P. Wheeler, M. Nowotny, N. Gilbert, T. Chandra, M.A.M. Reijns, A.P. Jackson, cGAS surveillance of micronuclei links genome instability to innate immunity, Nature 548 (7668) (2017) 461–465.

[48] M. Motwani, S. Pesiridis, K.A. Fitzgerald, DNA sensing by the cGAS-STING pathway in health and disease, Nat. Rev. Genet. 20 (11) (2019) 657–674.

[49] T.J. Hayman, M. Baro, T. MacNeil, C. Phoomak, T.N. Aung, W. Cui, K. Leach, R. Iyer, S. Challa, T. Sandoval-Schaefer, B.A. Burtness, D.L. Rimm, J.N. Contessa, STING enhances cell death through regulation of reactive oxygen species and DNA damage, Nat. Commun. 12 (1) (2021) 2327.

[50] Y.S. Tan, K. Sansanaphongpricha, Y. Xie, C.R. Donnelly, X. Luo, B.R. Heath, X. Zhao, E. Bellile, H. Hu, H. Chen, P.J. Polverini, Q. Chen, S. Young, T.E. Carey, J.E. Nor, R.L. Ferris, G.T. Wolf, D. Sun, Y.L. Lei, Mitigating SOX2-potentiated immune escape of head and neck squamous cell carcinoma with a STING-inducing nanosatellite vaccine, Clin. Cancer. Res. 24 (17) (2018) 4242–4255.

[51] C. Wu, W. Chen, F. Yu, Y. Yuan, Y. Chen, D.R. Hurst, Y. Li, L. Li, Z. Liu, Long noncoding RNA HITTERS protects oral squamous cell carcinoma cells from endoplasmic reticulum stress-induced apoptosis via promoting MRE11-RAD50-NBS1 complex formation, Adv. Sci. 7 (22) (2020).

[52] Y. Zhao, W. Kong, P. Wang, G. Song, Z.L. Song, Y. Yang, Y. Wang, B. Yin, P. Rong, S. Huan, X.B. Zhang, Tumor-specific multipath nucleic acid damages strategy by symbiosed nanozyme@enzyme with synergistic self-cyclic catalysis, Small 17 (28) (2021) e2100766.

[53] C. Zhang, G. Shang, X. Gui, X. Zhang, X.C. Bai, Z.J. Chen, Structural basis of STING binding with and phosphorylation by TBK1, Nature 567 (7748) (2019) 394–398.

[54] S. Liu, X. Cai, J. Wu, Q. Cong, X. Chen, T. Li, F. Du, J. Ren, Y.T. Wu, N.V. Grishin, Z.J. Chen, Phosphorylation of innate immune adaptor proteins MAVS, STING, and TRIF induces IRF3 activation, Science 347 (6227) (2015) aaa2630.

[55] L. Zhou, B. Hou, D. Wang, F. Sun, R. Song, Q. Shao, H. Wang, H. Yu, Y. Li, Engineering polymeric prodrug nanoplatform for vaccination immunotherapy of cancer, Nano Lett. 20 (6) (2020) 4393–4402.

[56] L. Deng, H. Liang, M. Xu, X. Yang, B. Burnette, A. Arina, X.D. Li, H. Mauceri, M. Beckett, T. Darga, X. Huang, T.F. Gajewski, Z.J. Chen, Y.X. Fu, R.R. Weichselbaum, STING-Dependent cytosolic DNA sensing promotes radiation-induced type i interferon-dependent antitumor immunity in immunogenic tumors, Immunity 41 (5) (2014) 843–852.

[57] L. Corrales, V. Matson, B. Flood, S. Spranger, T.F. Gajewski, Innate immune signaling and regulation in cancer immunotherapy, Cell Res. 27 (1) (2017) 96–108.

[58] C.S. Garris, J.J. Luke, Dendritic cells, the t-cell-inflamed tumor microenvironment, and immunotherapy treatment response, Clin. Cancer Res. 26 (15) (2020) 3901–3907.

[59] Z. Zhang, W. Sang, L. Xie, W. Li, B. Li, J. Li, H. Tian, Z. Yuan, Q. Zhao, Y. Dai, Polyphenol-based nanomedicine evokes immune activation for combination cancer treatment, Angew Chem. Int. Ed. 60 (4) (2021) 1967–1975.

[60] Q. Chen, Y. He, Y. Wang, C. Li, Y. Zhang, Q. Guo, Y. Zhang, Y. Chu, P. Liu, H. Chen, Z. Zhou, W. Zhou, Z. Zhao, X. Li, T. Sun, C. Jiang, Penetrable nanoplatform for "cold" tumor immune microenvironment reeducation, Adv. Sci. 7 (17) (2020) 2000411.

[61] V.M. Kho, V.E. Mekers, P.N. Span, J. Bussink, G.J. Adema, Radiotherapy and cGAS/STING signaling: Impact on MDSCs in the tumor microenvironment, Cell Immunol. 362 (2021).

[62] C.X. Zhang, S.B. Ye, J.J. Ni, T.T. Cai, Y.N. Liu, D.J. Huang, H.Q. Mai, Q.Y. Chen, J. He, X.S. Zhang, Y.X. Zeng, J. Li, J. Cui, STING signaling remodels the tumor microenvironment by antagonizing myeloid-derived suppressor cell expansion, Cell Death Differ. 26 (11) (2019) 2314–2328.

[63] L. Schadt, C. Sparano, N.A. Schweiger, K. Silina, V. Cecconi, G. Lucchiari, H. Yagita, E. Guggisberg, S. Saba, Z. Nascakova, W. Barchet, M. van den Broek, Cancer-cell-intrinsic cGAS expression mediates tumor immunogenicity, Cell Rep. 29 (5) (2019) 1236–1248 e7.

[64] M. Yarchoan, A. Hopkins, E.M. Jaffee, Tumor mutational burden and response rate to PD-1 inhibition, New Engl. J. Med. 377 (25) (2017) 2500–2501.

[65] H. Tang, Y. Liang, R.A. Anders, J.M. Taube, X. Qiu, A. Mulgaonkar, X. Liu, S.M. Harrington, J. Guo, Y. Xin, Y. Xiong, K. Nham, W. Silvers, G. Hao, X. Sun, M. Chen, R. Hannan, J. Qiao, H. Dong, H. Peng, Y.X. Fu, PD-L1 on host cells is essential for PD-L1 blockade-mediated tumor regression, J. Clin. Invest. 128 (2) (2018) 580–588.

[66] S.A. Oh, D.C. Wu, J. Cheung, A. Navarro, H.Z. Xiong, R. Cubas, K. Totpal, H. Chiu, Y. Wu, L. Comps-Agrar, A.M. Leader, M. Merad, M. Roose-Germa, S. Warming, M.H. Yan, J.M. Kim, S. Rutz, I. Mellman, PD-L1 expression by dendritic cells is a key regulator of T-cell immunity in cancer, Nat. Cancer 1 (7) (2020) 681.

[67] Y. Liu, J. Zugazagoitia, F.S. Ahmed, B.S. Henick, S.N. Gettinger, R.S. Herbst, K.A. Schalper, D.L. Rimm, Immune Cell PD-L1 colocalizes with macrophages and is associated with outcome in PD-1 pathway blockade therapy, Clin. Cancer Res. 26 (4) (2020) 970–977.

[68] T.B.M. Permata, Y. Hagiwara, H. Sato, T. Yasuhara, T. Oike, S. Gondhowiardjo, K.D. Held, T. Nakano, A. Shibata, Base excision repair regulates PD-L1 expression in cancer cells, Oncogene 38 (23) (2019) 4452–4466.

[69] T. Sen, B.L. Rodriguez, L. Chen, C.M.D. Corte, N. Morikawa, J. Fujimoto, S. Cristea, T. Nguyen, L. Diao, L. Li, Y. Fan, Y. Yang, J. Wang, B.S. Glisson, Wistuba II, J. Sage, J.V. Heymach, D.L. Gibbons, L.A. Byers, Targeting DNA damage response promotes antitumor immunity through STING-mediated T-cell activation in small cell lung cancer, Cancer Discov. 9 (5) (2019) 646–661.